

Non-Symmetric Behavior of High Strain Composite Tape Spring Hinges for Folding Structures

JoAnna Fulton* and Hanspeter Schaub†

University of Colorado at Boulder, Boulder, CO, 80309-0431, USA

A method for studying the free deployment dynamics of folding spacecraft structures that uses multi-body dynamics and a simplified hinge representation is being explored to numerically study large scale deployment dynamics. In the approach, fold panels are treated as rigid bodies and the flexible hinges are represented by internal forcing functions. A high strain composite tape spring hinge is a novel actuator for free deployment, however without additional constraining mechanisms, such a hinge can display non-symmetric, three dimensional behavior. The focus of this paper is to develop a hinge model that represents the forces and torques of the hinge on the bodies as a function of the hinge's full degrees of freedom, relative position and orientation states. Data for force and torque is acquired through finite element simulations and an experimental test bed. Data values of the two methods are compared. Nonlinear regression fits candidate polynomials to the simulation data and the effectiveness of the fits are explored.

I Introduction

THE size and weight constraints of launch vehicles have inspired the development of innovated deployable spacecraft structures technologies.¹ An emerging area in this field takes inspiration from origami folding techniques to stow flat structures with large area to size ratio relative to the spacecraft bus, such as solar² and phase³ arrays, star occulters,⁴ and reflectors.^{5,6} A central challenge for this concept is the deployment dynamics and deployment actuation of the folded structure and spacecraft system. A novel lightweight solution is to integrate strain energy hinges to facilitate folding and actuate the deployment.⁷ High strain composite tape spring hinges are an intriguing innovation in hinge technology for deployable space structures. Compared to standard piano hinges, these hinges are lightweight, eliminate rotational mechanical contact surfaces, and are self-actuating. A simple example of how this concept could be implemented physically using the miura-ori pattern is illustrated in Figure 1, and it is noted that even with minimal hinge actuation, 10 hinges are used to actuate the 12 panel assembly. Of additional note is that the thickness of the fold panels requires some minimal gap thickness between each panel to facilitate folding, enabling small displacements in multiple degrees of freedom. Deployment dynamics of such a system would typically be studied through finite element analysis (FEA). However, for a structure with multiple high strain composite hinges, FEA modeling would require significant computational time and skill. This limits the ability to explore parameter design spaces and iterate towards more optimal solutions. An alternative method for studying the system dynamics that uses multi-body dynamics and a simplified hinge representation has been proposed.⁸ In this approach, fold panels are treated as rigid bodies and the flexible joints are represented by internal forcing functions. A similar concept of representing a complex mechanical hinge with a contact model for dynamics modeling has been demonstrated using an integrated finite element and multibody software.⁹ Here, a model to represent the hinge mechanics is designed as a function of the hinge's full degrees of freedom, relative position and orientation states. Data containing reaction forces and torques at the hinge body connection points are obtained from FEA simulation and experimental studies for hinge configurations containing non-symmetric displacements, and they are compared for validation purposes. A nonlinear regression is applied to fit the simulated data to polynomials and the efficacy of this fit is assessed. The approach is shown to provide an approximation that may enable sufficient deployment dynamics simulation accuracy without a full FEA simulation of the system.

*Graduate Research Assistant, Aerospace Engineering Sciences, 431 UCB, Colorado Center for Astrodynamics Research, Boulder, CO, 80309-0431, and AIAA Student Member.

†Glenn L. Murphy Chair of Engineering, Aerospace Engineering Sciences, 431 UCB, Colorado Center for Astrodynamics Research, Boulder, CO, 80309-0431, and AIAA Associate Fellow

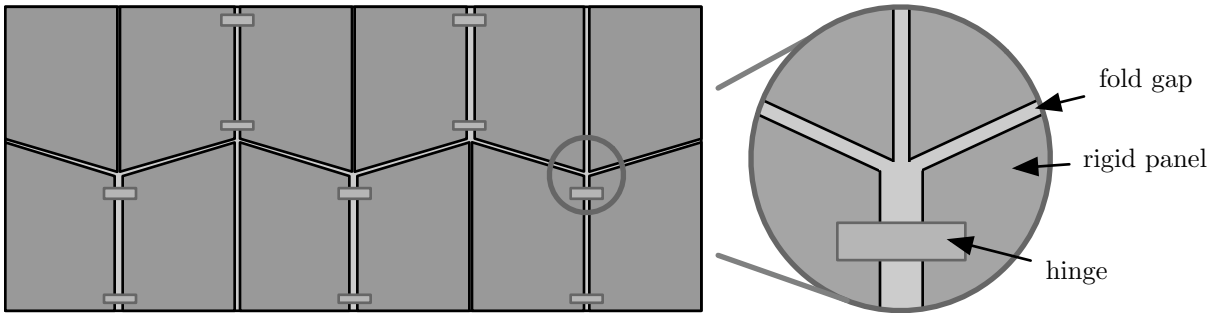


Figure 1: Example of a closed-chain structure with tape spring hinge integration.

I.A High Strain Composite Tape Spring Hinges

I.A.1 Literature Review and Motivation

Several research studies characterize the moment-curvature behavior of tape spring hinges for various materials assuming the hinge folds symmetrically, meaning through only one rotational degree of freedom (DOF). Typically, the equal-sense and opposite-sense bending moment is characterized through theoretical analysis and experimental testing.^{10,11} Here, equal-sense refers to a fold where the open cross sections face each other and opposite-sense is a fold where the open cross sections face away, as is consistent with the tape spring literature. There has been further interest in characterizing the behavior of a diagonally folded hinge.¹² These studies provide fundamental understanding of a hinge's structural mechanics behavior, focusing on failure and stiffness, and demonstrate their correlation with mechanics theory. However, here, the objective is to reframe the hinge as a dynamic actuator and capture the deployment behavior of a system as actuated by the hinge. The tape spring introduces unique challenges from this perspective. A typical fold joint is treated as a single DOF revolute joint where the attachment points on each connected body are coincident and have one relative rotation. Under certain assumptions, the symmetric behavior of the tape spring hinge can be modeled as a single rotation where the moment-curvature behavior describes the internal torque due to the hinge. However, the connection points are separated by the length of the hinge and will be displaced from each other over the deployment. The actual force and torque response of the hinge will depend on the loading of either side of the hinge, and small displacements from the nominal configuration may introduce significant force and torque responses. Therefore, the established moment-curvature approach is not sufficient for the modeling fidelity desired here, and a study of force and torque responses due to non-symmetric behavior is conducted. The phenomenon of undesirable non-symmetric configurations in the tape spring hinge fold is not well studied. Here, non-symmetric behavior refers to any change in position and orientation that does not follow the nominal fold rotation, as is illustrated in Figure 3. To guarantee symmetric behavior, additional components must be included in a hinge assembly to constrain the hinge, which can add mass and complexity where lightweight simplicity is desired. Such solutions are not addressed here. Inclusion of multiple independent state variables in this study makes it difficult to approach the problem with classical theory, therefore, to study this phenomenon, numerical and experimental techniques are employed.

High strain composites are a novel class of flexible material with great potential for spacecraft deployable structures. The material is able to accommodate large deflections and experience high strain without failure or plastic deformation, while providing high structural stiffness for low mass. However there are challenges to implementing these materials. Modeling and predicting the behavior is difficult due to nonlinearity, manufacturing variability, and complex geometry. For these reasons, an experimental test is needed for qualification of the numerical simulation data and is included in this study.

I.A.2 Tape Spring Hinge Properties and Geometry

The geometry of the structure in the folded and unfolded state is determined by the parameters of the tape spring geometry. The material thickness t , radius of cross sectional curvature R , and cross section arc length a are free design parameters that are fixed to specific material samples in this study. Two hinge material samples are provided in this study, and the parameters of the samples are recorded in Table 1. The first material sample is a high strain composite with a single layer of 0 deg unidirectional fibers sandwiched between 45 deg plain weave carbon fiber, a material recently developed for high strain composite spacecraft deployable booms. The second material sample is constructed of the same base materials but has double the layers of unidirectional fibers. These additional fibers are included to increase the strain energy and deployment torque of the hinge. The properties of these materials are derived from

Table 1: Hinge geometry for tested samples and matching FEA models

sample	x-section radius R , (mm)	arc length a , (mm)	thickness t , (mm)	length L , (mm)
[45PW ₁₂ /0 ₁₂ /45PW ₁₂]	15.875	35	0.9	150
[45PW ₁₂ /0 ₁₂ /0 ₁₂ /45PW ₁₂]	15.875	35	0.9	150

tensile test data and classical laminate theory and are provided by the NASA Langley Research Center. The tape spring length, L , is designed to minimize fold profile and non-symmetric fold range or flexibility. The capacity for non-symmetric fold behavior increases as the length of the flexible hinge section is increased. However, the hinge must be long enough for the cross section to transition from the stable c-shape to the flat fold without material failure. Therefore, the minimum allowable length of the tape spring must be determined. The high strain materials applied here were observed to have a maximum tensile strain of 1.7%, and a maximum allowable strain is set to 1.2% to allow for some factor of safety. A quick study is conducted to observe the maximum principle strains occurring in the tape spring for various lengths when the hinge undergoes a nominal fold to 90 deg using an FEA simulation. The results are shown in Figure 2 for both materials undergoing an equal sense fold, and a length of 150 mm is selected for this study. This is done for a tape spring with 20 mm long clamps attached at each end point, resulting in a shorter effective composite hinge section.

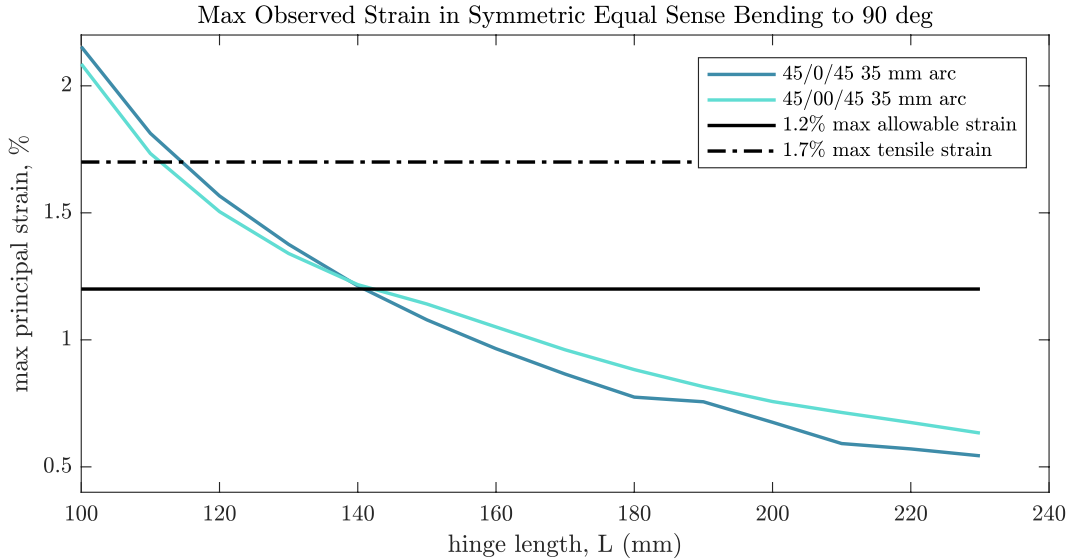


Figure 2: Maximum principle strain in the HSC tape spring as a function of length.

II Rigid Body Dynamics and the 6 State Hinge Model

The tape spring hinge is represented in the rigid body dynamics simulations as an internal forcing function in terms of the position and orientation of the hinge connection points. This concept is illustrated in Figure 3, where the fixed end points of the hinge are each assigned a reference frame, \mathcal{A}_0 and \mathcal{A}_1 , the reaction forces from the hinge are denoted N_0 and N_1 , and the reaction moments are denoted as M_0 and M_1 . These mechanics are modeled as functions of the relative position, δ , and orientation of frame \mathcal{A}_0 with respect to \mathcal{A}_1 . The hinge model is developed to be compatible with a preexisting multi-body dynamics framework based on the Articulated Body Forward Dynamics approach.¹³ This approach de-constructs a system of linked rigid bodies by defining the interactions across the hinge connecting an outbound body to an inbound body through relative coordinates, and selecting these as the generalized coordinates of the dynamics model. The framework of the algorithm then calculates the system dynamics having only needed the relative hinge definitions and rigid body properties. To provide consistency with this, the generalized coordinates are selected to be the displacement of the relative hinge frame coordinates and the relative orientation

$$\mathbf{q} = \begin{bmatrix} \theta(\mathcal{A}_0, \mathcal{A}_1) \\ \delta(\mathcal{A}_0, \mathcal{A}_1) \end{bmatrix} \quad (1)$$

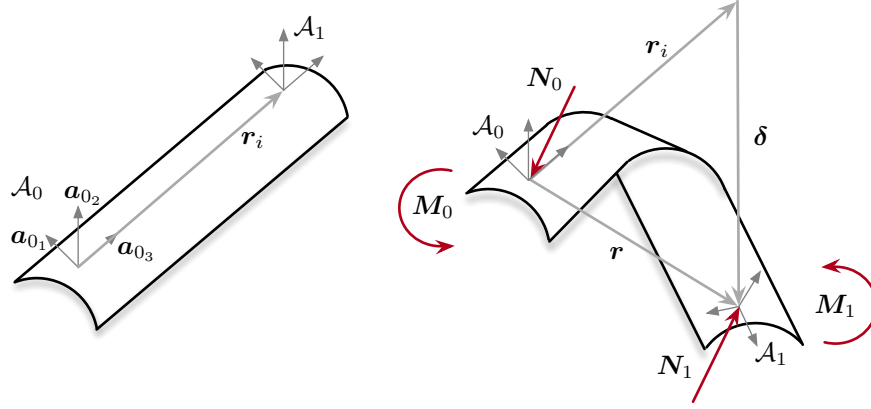


Figure 3: Definitions for a tape spring hinge in deployed (left) and non-symmetric (right) configurations.

For this analysis, all dynamics quantities are expressed with respect to the hinge origin frame defined as the inbound frame, \mathcal{A}_0 . This lends insight into how the hinge affects any inbound body directly, and how an outbound body is affected relative to the inbound body. This information can be easily transformed to desired frames as needed. The hinge origin frame is oriented on the hinge such that the third axis, \mathbf{a}_{03} is pointed down the length of the hinge, \mathbf{a}_{02} is normal to the hinge cross section, and \mathbf{a}_{01} completes the right hand convention. The relative orientation $\theta(\mathcal{A}_0, \mathcal{A}_1)$ contains 3 – 2 – 1 Euler Angles for ease of interpretation and because the second axis, where the 90 degree Euler angle singularity resides, can be oriented with an axis which does not accommodate significant relative deflection. The \mathcal{A}_1 frame is oriented identically to the \mathcal{A}_0 frame when the hinge is deployed in the zero energy state. The displacement of the relative hinge frame coordinates, δ , is selected over the relative position, \mathbf{r} , to better correlate the physical behavior with the numerical fit. The relation of these vectors is displayed in Figure 3, defined as

$$\delta = \mathbf{r} - \mathbf{r}_i \quad (2)$$

Then the generalized forces and torques acting at frame \mathcal{A}_0 are written as a function of the relative coordinates across the hinge frames, in spatial notation, as

$$\mathbf{f}_0(\mathbf{q}) = \begin{bmatrix} \mathbf{N}_0 \\ \mathbf{M}_0 \end{bmatrix} = \begin{bmatrix} N_{01} \\ N_{02} \\ N_{03} \\ M_{01} \\ M_{02} \\ M_{03} \end{bmatrix} \quad (3)$$

The common assumption for hinge force and torque models is that the force and torque are acting in equal but opposite direction on each of the connected rigid bodies at the connection frames. While a quick free body analysis of Figure 3 verifies this to be true for the force, the moment balance introduces something new. The summation of moments at either frame will require the torque due to the reaction force and the relative position of the frames be included. Therefore, the spatial force at frame \mathcal{A}_1 can be written in terms of only the force and torque at frame \mathcal{A}_0 as

$$\mathbf{f}_1(\mathbf{q}) = \begin{bmatrix} \mathbf{N}_1 \\ \mathbf{M}_1 \end{bmatrix} = \begin{bmatrix} -\mathbf{N}_0 \\ -\mathbf{M}_0 - \mathbf{r} \times \mathbf{N}_0 \end{bmatrix} \quad (4)$$

II.A Model Estimation and Nonlinear Regression

Equation 4 indicates that the force and torque applied to the rigid bodies can be determined for both sides of the hinge using a model of only one set of forces and torques. Therefore, the objective is to determine adequate models for the six entries of $\mathbf{f}_0(\mathbf{q})$. There are several options for determining response functions that include large multi-variable data sets. Simple approaches include using a look-up table or interpolation between data points. However, these will not necessarily provide insight into predictor variable relationships and cannot be further manipulated. Therefore, a function fit is desired. A polynomial containing both first order and second order coupled polynomials is first proposed

for capturing the non-symmetric relationships.

$$p(\mathbf{q}) = \sum_{i=1}^6 a_i q_i + \sum_{j=1}^6 \sum_{k=1}^6 b_{jk} q_j q_k \quad (5)$$

Equation 5 contains 27 unknown coefficients. In this approach, each of the force and torque data sets is first fit using the full polynomial, and the resulting coefficients are then analyzed to eliminate expressions that have insignificant contributions. The objective is to reduce the polynomial to the smallest, and therefore computationally most efficient, expression while still providing an adequate fit to the data. Additionally, the coefficients for these second order cross-coupled terms can be used to interpret the significance of the generalized state variables. It's suggested from the literature that the nominal fold produces a pure moment in the symmetric case, and this moment can be represented using a 7th order polynomial.¹⁰ Then for the moment about α_{0_1} , the initial polynomial includes higher order terms for the nominal rotation, as in

$$M_{0_1} = p(\mathbf{q}) + \sum_{i=3}^7 c_i q_1^i \quad (6)$$

A non-linear regression approach is best suited for the nonlinear, multivariate model functions in Equations 5 and 6. The Statistics and Machine Learning Toolbox published for Matlab is used to fit and evaluate the models. The quality of the fit is evaluated several means. The toolbox is further used to acquire an R-squared estimate, the root mean squared error (RMSE), and the histograms of the raw residuals. The coefficient of determination, R-squared, is meant to indicate how much of the variation in the response is captured by they model and is expressed on a scale of 0 to 1 where the fit is better the closer it is to 1. For a non-linear regression, the R-squared value is not entirely trustworthy but is considered here as for initial evaluations. The root mean squared error is the average standard deviation of the fit and the histograms provide a full picture of how variable the fit is. The effectiveness of each coefficient is evaluated by calculating the coefficient's p-value, a measure that reflects how much the function is influenced by the inclusion of the coefficient. Coefficients and their corresponding polynomial terms are eliminated using this measure and the effect on the R-squared and RMSE values are monitored for improvements.

II.B Potential Function

Validation of a dynamics model starts with the conservation of energy and conservation of momentum principles. These provide a standard check that the internal forces and torques have been correctly implemented before applying external forces and torques to the system. For modeling a free deployment that is actuated by internal strain energy, this validation is crucial and for complex forcing functions, becomes non-trivial. The desire for a potential function motivates the use of a fit function over a look-up table or interpolation approach to the data processing. A potential function can be derived from the work-energy principle, where for a tape spring, the potential, U , at the final, deployed point, \mathbf{x}_f , is known to be zero, as

$$W = \int_p \mathbf{F}(\mathbf{x}) d\mathbf{x} = U(\mathbf{x}_i) - U(\mathbf{x}_f) = U(\mathbf{x}_i) \quad (7)$$

where \mathbf{x}_i is the starting point on path p and $\mathbf{F}(\mathbf{x})$ is any forcing function with a conservative vector field. The polynomials selected in Equations 5 and 6 are trivially integrable over \mathbf{q} , and therefore their implementation as conservative internal force functions can be evaluated using their corresponding potential as desired.

II.C Asymmetry Definitions

The space of all possible hinge configurations is intractable at initial consideration, and so a subspace of most likely configurations that is also observable is identified. Three primary asymmetric configurations are identified as deviations from the symmetric case. The deviations considered ranged from 5-10 degrees, deviations that are too large to be negligible but small enough that they are feasible. Each deviation from the symmetric case is observed separately, and not compounded, in attempt to isolate the independent variables from each other. The bounds for these cases are listed in Table 2 for both the simulation and experimental cases, in both the equal and opposite sense fold directions. A shorthand notation for the configurations is also introduced and defined in this Table.

Identifying these bounds is the primary challenge to studying the asymmetric behavior and strongly dictates the outcome of the model fits. Three primary displacement cases are selected for this study based on the obvious configurations and are not representative of all possible configurations. The bounds for the non-symmetric configurations

Table 2: Asymmetric configuration constraints used to generate Abaqus (A) and experimental (S) data sets in both equal (E) and opposite (O) folds.

Case	θ_1 sym (deg)	θ_1 offset (deg)	θ_2 (deg)	θ_3 (deg)	δ_1 (mm)	δ_2 (mm)	δ_3 (mm)
AE0	0 – 180	0	0	0	0	0	free
AE1	30 – 180	± 10	0	0	0	0	free
AE2	30 – 180	0	0	± 10	0	0	free
AE3	30 – 180	0	0	± 10	$f(\theta_3)$	$f(\theta_3)$	0
SE0	0 – 140	0	0	0	0	0	$f(\theta_1)$
SE1	100 – 140	± 10	0	0	0	0	$f(\theta_1)$
SE2	100 – 140	0	0	± 10	0	0	$f(\theta_1)$
AO0	0 – 180	0	0	0	0	0	free
AO1	90 – 180	± 10	0	0	0	0	free
AO2	90 – 180	0	0	± 5	0	0	free
SO0	0 – 140	0	0	0	0	0	$f(\theta_1)$
SO1	90 – 140	± 10	0	0	0	0	$f(\theta_1)$
SO2	90 – 140	0	0	± 10	0	0	$f(\theta_1)$

are designed to approach the physical bounds of the hinge. The experimental fixture is designed to implement these measured deviations in a single system, therefore limiting the number of possible configurations. The resulting design is described in detail in section IV. Future work could investigate measuring additional asymmetries through multiple fixtures. These deviations are expressed with respect to the \mathcal{A}_0 frame as described in previous sections. The tape spring behavior is subject to a few physical constraints that are used to define these bounds and the relationships within the states. For example, the relationship between the orientation about α_{01} and the displacement δ_3 can be expressed generally, for any non-symmetric relative angles by considering the law of cosines and by assuming the radius of curvature over the fold bend is known.

III Finite Element Model Overview

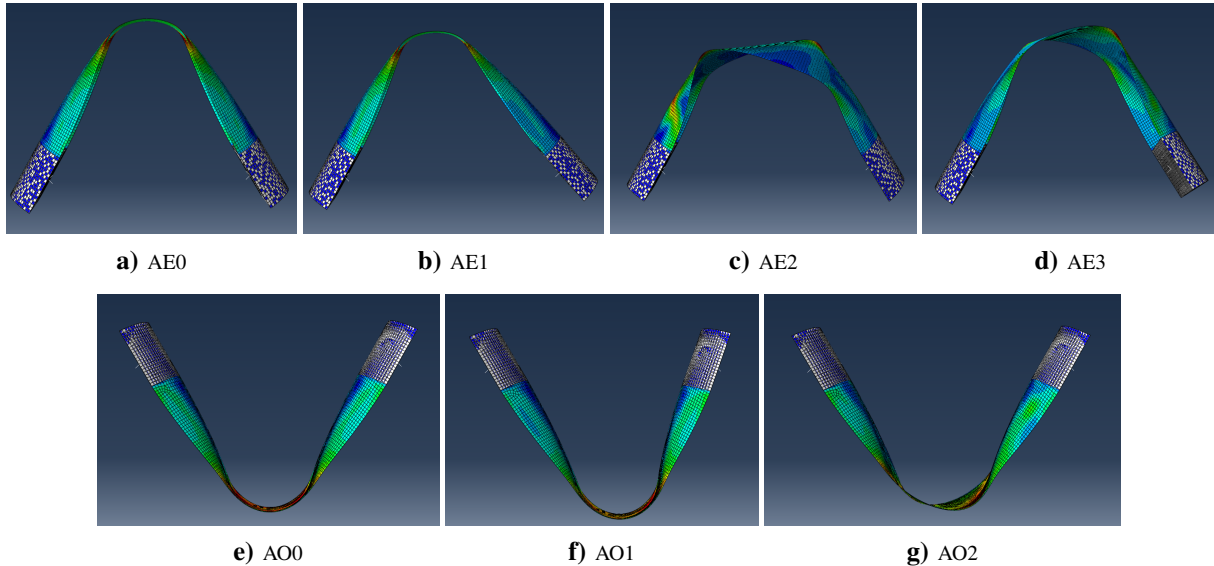


Figure 4: Examples of displacements implemented in ABAQUS where the symmetric angle is ± 60 deg.

Finite element analysis simulations are built in ABAQUS 6.14. The hinge is represented as a shell with elastic behavior defined by engineering constants. The fixtures are represented as discrete rigid parts, are 20 mm in length, and are assembled and constrained using tie constraints. Four node shell (S4R) elements are meshed on the hinge shell using a 1 mm mesh. The asymmetric configurations are implements as displacement and rotation boundary conditions

in static/general steps. Each range of asymmetric configurations is explored as a separate step enforced on an initially symmetric configuration. An asymmetric data set is generated for each primary fold angle, θ_1 , at increments of 5 degrees, resulting in 16 equal sense and 10 opposite sense data sets for each material. Figure 4 shows example profiles for the equal sense and opposite sense cases and with non-symmetric deviations, with a no added deformation scaling.

Designing the displacement and rotation boundary conditions such that the simulations converge without error is not trivial and not easily automated. The approach here is to fix the inbound hinge frame to zero displacements and to apply displacements and necessary degrees of freedom to the outbound frame. Then the reaction forces, reaction moments, displacement, and rotational displacements are reported for the reference points representative of the hinge reference frames. The hinge reference frame is centered on the hinge endpoint fixture, and is mirrored in the design of the experiment. The opposite sense simulation required an additional step to bring the hinge pass the initial snap through phase. This was done by first pressing the shell flat with a rigid pin, and then removing the pin and continuing to the symmetric fold configurations. These steps are excluded from the data. The full range of symmetric fold angle data is acquired despite the pin by stepping through the fold angle constraints in reverse, from fully folded to fully deployed.

IV Experimental Testbed Overview

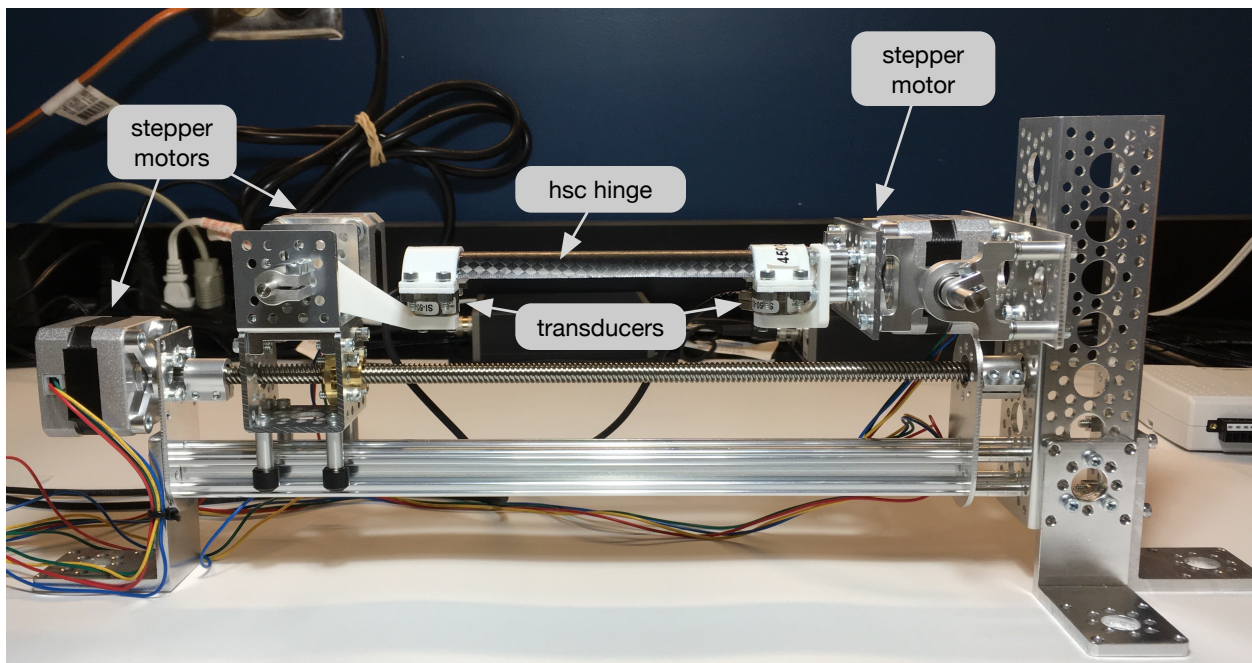


Figure 5: Components of the experiment testbed set up.

A mechanical testbed is designed to configure and control the asymmetric displacements, and a diagram of this design is presented in Figure 5. Two ATI six-axis force/torque transducers are used at the reference frames on the hinge to directly measure the full force/torque profile. The transducers are calibrated for torque measurements of 500 N-mm with 1/16th N-mm resolution and forces of 50 N in plane and 70 N out of plane with 1/80th N resolution. These sensors are aligned with the hinge such that the measurement frame of the sensor is coincident and orthogonally aligned to the hinge reference frames \mathcal{A}_0 and \mathcal{A}_1 . The data from these hinges are then transformed into the frame alignments defined in Figure 3. An NI Labview program is used to interface with the transducers through an NI USB-6218 data acquisition card. The hinge configuration is controlled using multiple stepper motors and a SparkFun RedBoard, also interfaced through the Labview program with identical timing. The hinge configuration is not observed through external means, but is derived through the stepper motor count. The stepper motors are controlled using microstepping, with a resolution of 0.225 degrees per step. The left reference point of the hinge is mounted to a cart controlled through a smooth linear rail and the rotation about \mathbf{a}_{0_1} is controlled by an additional motor. The right reference point is mounted to a freely rotating axis parallel to \mathbf{a}_{0_1} , and the twist about the hinge length axis is controlled with a third motor. A fourth motor is available to twist the hinge point along the $\mathbf{a}_{1_1} - \mathbf{a}_{1_2}$ plane to acquire data on relative translation, but is not implemented in the presented data. A system of precision shafts, ball

bearing mounts, and standardized hardware provide smooth rotation, and this hardware is entirely manufactured by Actobotics. The tape spring hinges are each fixed at each end to 3D printed PLA plastic clamps using epoxy, and custom 3D printed mounts affix the hinge to the transducers. Custom mounting brackets are also 3D printed in PLA to mount the transducer assemblies to the testbed.

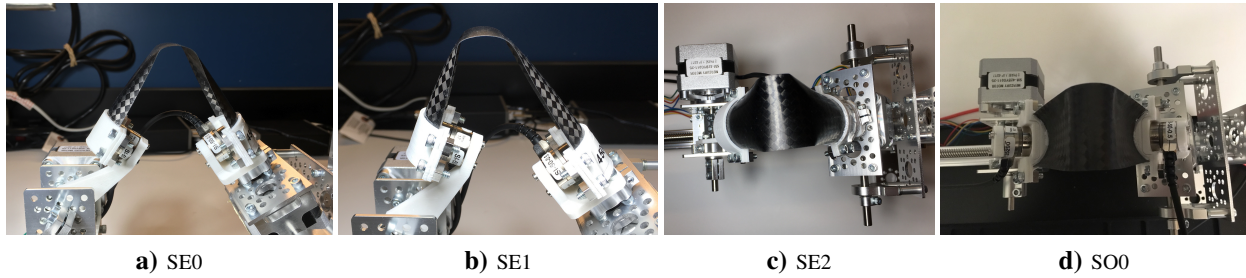


Figure 6: Examples of symmetric and non-symmetric displacements implemented in the experiments.

The experimental procedure is as follows. The hinge configuration is incremented into the symmetric configuration and data is sampled statically. Then each non-symmetric displacement is configured and sampled statically, resetting back to the symmetric configuration between each sample. Examples of the non-symmetric configurations are displayed in Figure 6. The geometry of the fixture must be taken into account when transforming the relative position and orientation data. The fixture creates an offset of the rotation axis from a_{0_1} of 42.5 mm at both sides of the testbed. The opposite sense configuration is achieved by flipping the coupon over using a modified mounting bracket, such that the hinge frames remain in the same position relative to the motor hubs. Several data samples are collected for a given configuration and are averaged to provide one sample per configuration.

V Results

V.A Symmetric Data Comparison

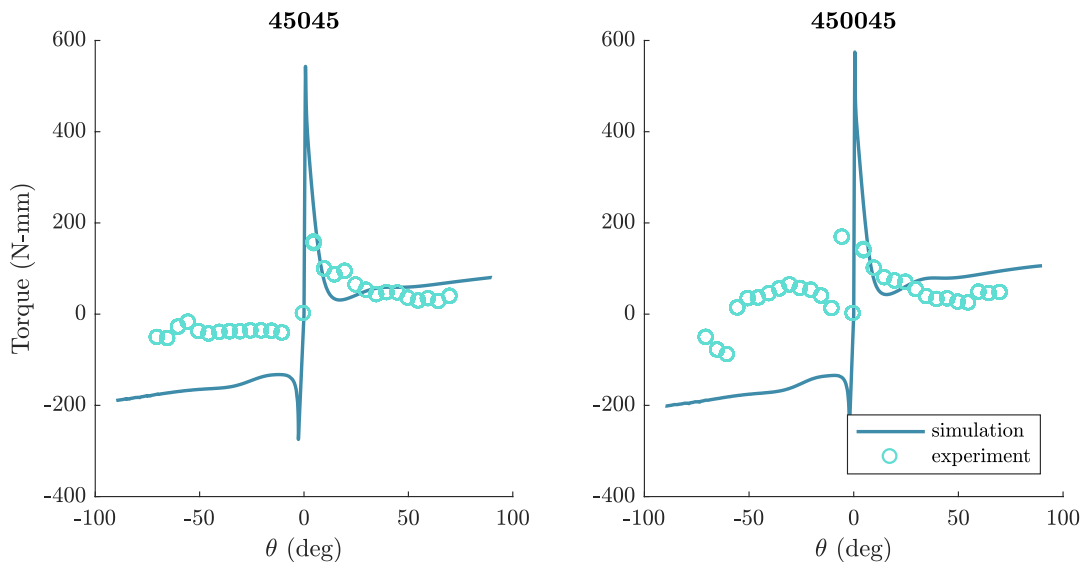


Figure 7: Moment response for the symmetric, 1 DOF moment-rotation.

Visualization of the fit is difficult due to the high number of independent state variables in the estimation. For an initial comparison, the symmetric case is considered due to its simplicity of visual and quantitative evaluation. The first axis moment is plotted in Figure 7 for both the experimental and simulated cases in both materials, where θ is the rotation from the initial position to the current position of the hinge frame. The experimental approach is not able to capture the moment peak at the initial fold, possibly due to small flexibilities in the testbed preventing the truly rigid response found in the simulations, and the trends do not strongly mimic each other. In particular, the opposite sense experimental data is significantly smaller than the general trend also deviates from the prediction. This indicates

there will be notable variation in the numerical and experimental models. Additionally, the experimental data shows significant third axis, or hinge normal, moments generated in this configuration, where no moment is expected. This is suspected to be due to imperfections in the layup construction, where the outer 45 degree plain weave plies are not truly aligned, and may also be due to unperceived misalignment of the testbed. This may imply that hinge performance relies heavily on hinge construction and undesired forces and torques are easily introduced to the system.

V.B Non-Symmetric Data Trends

The non-symmetric FEA numerical data predicts significant forces and torques generated from the hinge, suggesting that a slightly non-symmetric configuration can have significant impacts on deployment behavior. For certain cases, the forces are observed to be on the order of tens of Newtons and torques in the hundreds of Newton-millimeters, on the same order of magnitude as the symmetric torque. This trend is consistently observed in all the equal-sense and opposite-sense numerical FEA data sets. In Figure 8, the forces and torques for non-symmetric configurations of the 45/0/45 hinge are plotted for both the experimental and simulation data for the same symmetric angle cases, where only the boundary point of the simulated data is recorded. Similar trends are observed for the 45/00/45 case. The simulation data shows large torques on all axes are possible, and large forces are predicted for some equal sense bends.

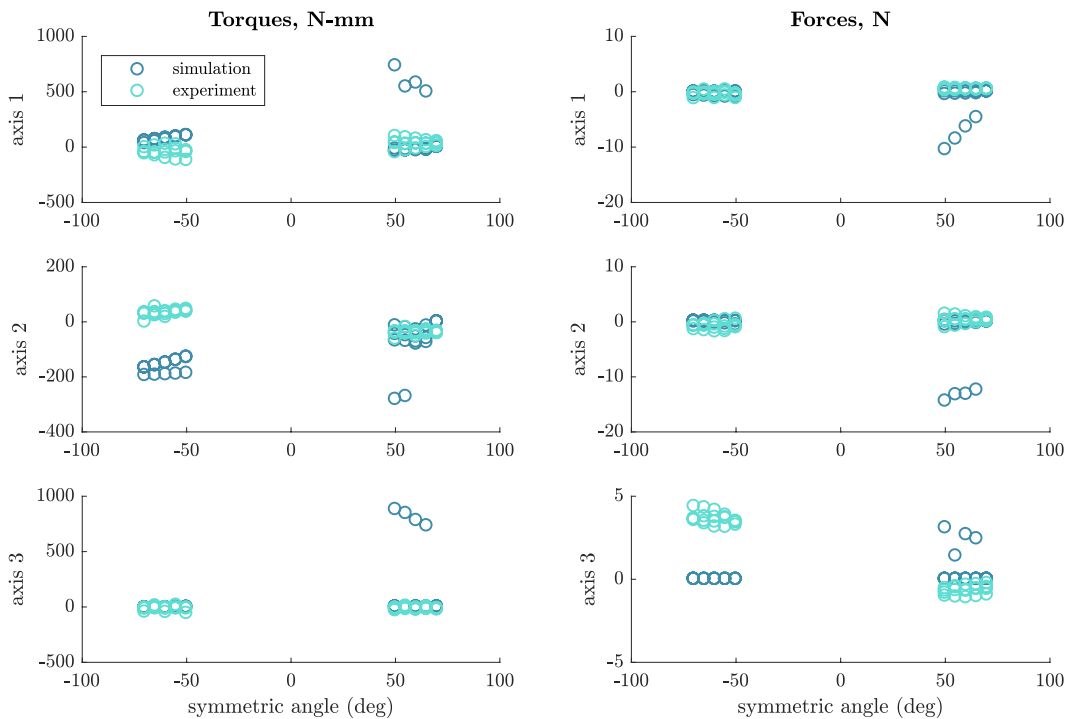


Figure 8: Forces and torques from non-symmetric configurations, recorded from both the experimental and simulated data of the 45/0/45 hinge. The symmetric angle is expressed as the hinge orientation from the initial flat configuration.

Comparing the experimental data with the simulation data reveals the experimental data does not exhibit any of the large force and torque behaviors. This is an unexpected result and warrants further study into the high strain composite hinge modeling and testing. The discrepancy suggests there are limitations of predicting the behavior of high strain materials undergoing large complex displacements using the material model implemented here, or that there is an unknown error in the simulation. The experimental data has further discrepancies, where for the third axis force, forces are observed where they were not predicted. These forces may have been introduced by the test fixture or by imperfections in the hinge build.

V.C FEA Nonlinear Regression Model Fits

V.C.1 Nominal Data Results

The nonlinear regression approach is not currently applied to the experimental data due to the low sample size of the data. The nonlinear regression is applied to the FEA data set and a reduced polynomial is iterated towards by evaluating the p-value of each coefficient for the full 45/0/45 material set with both equal and opposite sense folds. The same polynomials are applied to the full 45/00/45 set, where the coefficients are seen to have similar trends. The statistical results for each material are reported in Tables 3 and 4, and the corresponding estimated coefficients are reported in Tables 7 and 8 for completeness. The results show that the polynomial fits are not improved, but are also not greatly reduced, by reducing the number of polynomial terms. The statistics indicate that the fit is able to capture the majority of the trends, but is by no means a strong fit. The histograms in Figures 9 and 10 show that the data is not normally distributed and there are large residual outliers. This is true for both the force and torque cases. The large force and torque profiles from the asymmetries highlighted in Figure 8 are likely contributors to the difficulty of fitting this data. It's possible that the experimental data, or an FEA model that is reconciled with the data, would provide better results, where the experimental data did not measure these large force and torque responses. Fitting the primary deployment moment, M_{0_1} , is difficult to capture when including the asymmetric data. Evaluation of the coefficient p-values reveals that the higher order polynomial terms of Equation 6 do not contribute to improving the regression fit, and that $p(q)$ provides an equivalent fit. Therefore, these additional coefficients are removed and only $p(q)$ coefficients are reported in Tables 7 and 8.

Table 3: Statistics for the 45/0/45 FEA model fit functions.

statistic	M_{0_1}	M_{0_2}	M_{0_3}	N_{0_1}	N_{0_2}	N_{0_3}
full R-Squared	0.81	0.80	0.88	0.82	0.89	0.82
full RMSE	181	238	202	4.01	3.24	0.43
reduced R-Squared	0.81	0.79	0.88	0.81	0.88	0.79
reduced RMSE	182	240	203	4.05	3.25	0.46
num of coefficients	18	19	17	17	18	20

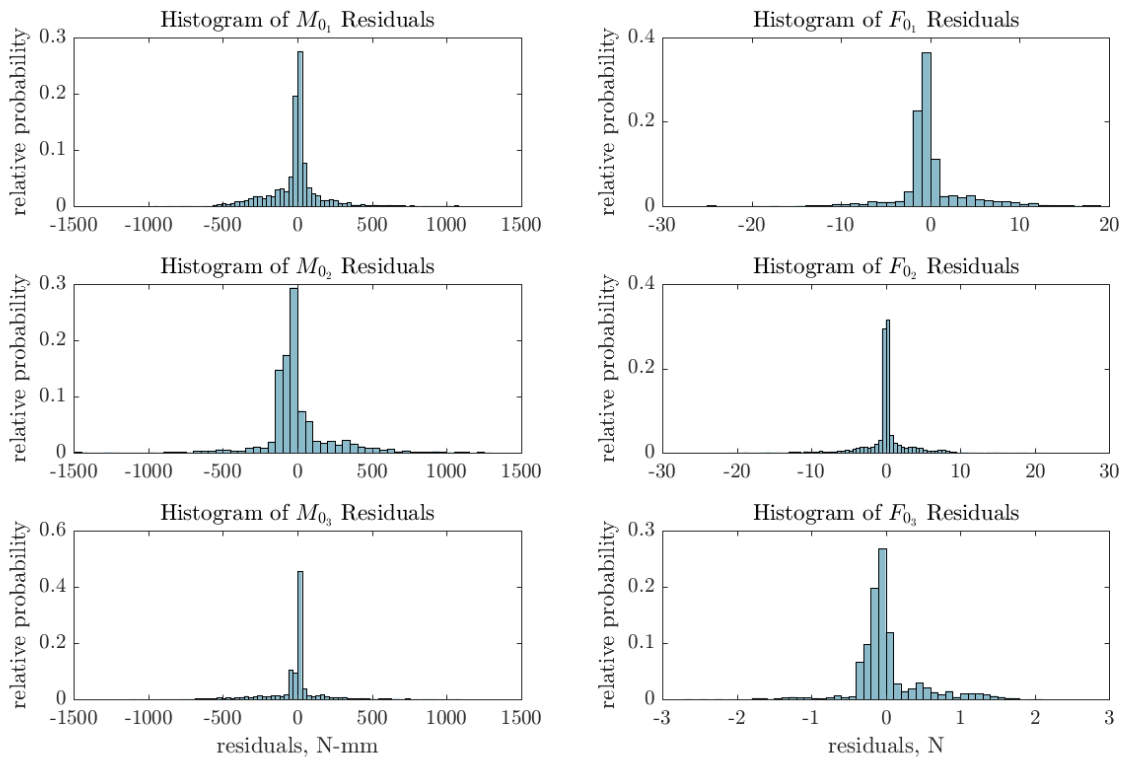
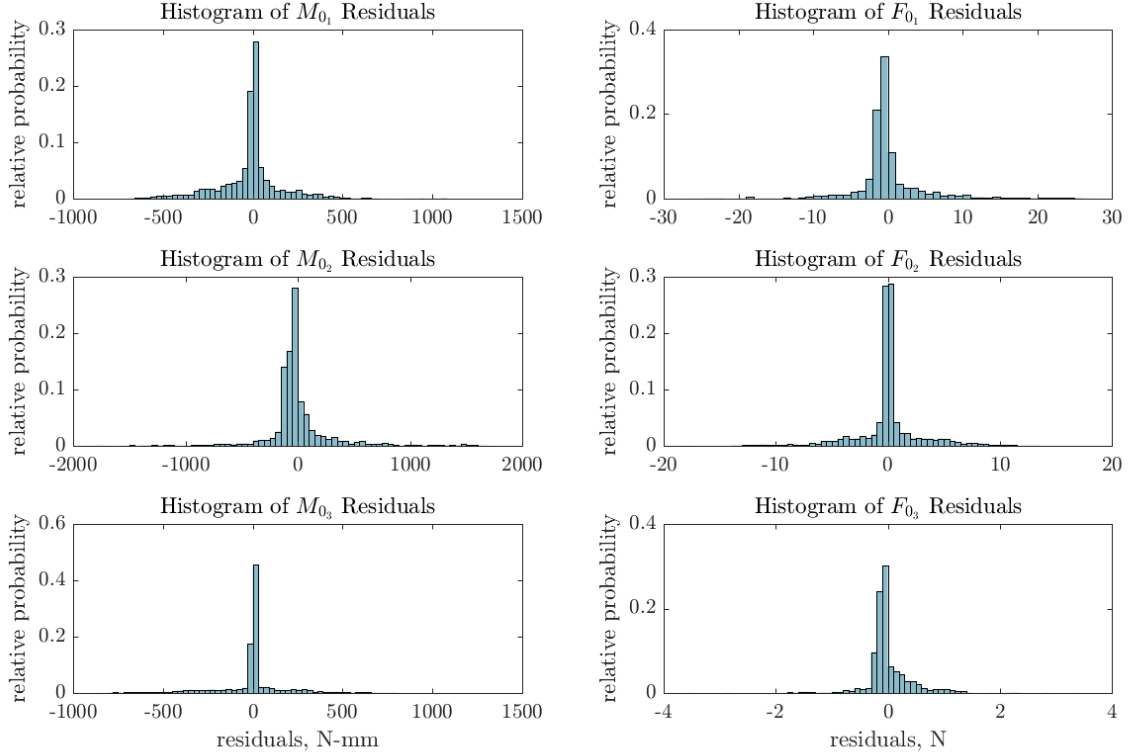


Figure 9: Fit function histograms for the 45/0/45 numerical simulations.

Table 4: Statistics for the 45/00/45 FEA model fit functions.

statistic	M_{0_1}	M_{0_2}	M_{0_3}	N_{0_1}	N_{0_2}	N_{0_3}
full R-Squared	0.81	0.71	0.88	0.76	0.90	0.88
full RMSE	177	278	188	4.53	2.88	0.36
reduced R-Squared	0.80	0.65	0.87	0.71	0.89	0.86
reduced RMSE	181	308	196	4.93	2.95	0.39
num of coefficients	18	19	17	17	18	20

**Figure 10: Fit function histograms for the 45/00/45 numerical simulations.**

VC.2 Additional Nonlinear Regressions

Attempts to improve the regression fit are made by examining alternative data sets, and two approaches are recommended. First, model improvements can be made by fitting the equal-sense and opposite-sense data individually and by using piecewise functions to join the models. The statistics for such a case are shown in Table 5, where all RMSE values are decreased and the opposite-sense fits have greatly improved RMSE and R-squared values. However this approach complicates the potential function validation, and is therefore not a desirable solution. The second approach to improving the model is to consider smaller asymmetric displacements for the data set. A numerical data set is generated in ABAQUS for cases where AE0 and AE1 are the same, but AE2 and AE3 are reduced to boundaries of $\theta = 5$ deg. Table 6 shows that the RSME and R-Squared values improve for both materials with this reduction. This improvement is as expected, where approximations are generally more accurate for smaller deviations. In addition to these approaches, expansions of Equation 5 beyond polynomial terms are explored. However, additions of trigonometric functions, logarithmic functions, or inverse polynomials are not found to significantly improve the fits, and therefore this approach is not currently recommended.

VI Conclusions and Future Work

This paper presents an approach for capturing the full six degree of freedom force and torque behavior of a high strain composite hinge in symmetric and non-symmetric configurations as a function of the hinge's six relative coordinates. Non-symmetric behavior is demonstrated to have significant force and torque profiles and therefore should be included in a robust dynamics model. Numerical predictions for force and torque are generated in ABAQUS for three

Table 5: Statistics for the 45/0/45 FEA model fit functions with full 27 coefficient polynomials using only equal or opposite sense data.

statistic	M_{0_1}	M_{0_2}	M_{0_3}	N_{0_1}	N_{0_2}	N_{0_3}
Equal R-Squared	0.84	0.88	0.93	0.90	0.92	0.91
Equal RMSE	127	191	121	3.12	1.89	0.29
Opposite R-Squared	0.98	0.97	0.99	0.97	0.99	0.98
Opposite RMSE	87.9	78.7	96.6	1.52	1.73	0.14

Table 6: Statistics for the fit functions with full 27 coefficient polynomials using non-symmetric boundaries of $\theta = 5$ deg for AE2 and AE3 ABAQUS data sets.

statistic	M_{0_1}	M_{0_2}	M_{0_3}	N_{0_1}	N_{0_2}	N_{0_3}
45/0/45 R-Squared	0.85	0.93	0.93	0.93	0.92	0.93
45/0/45 RMSE	145	130	138	2.29	2.44	0.21
45/00/45 R-Squared	0.85	0.93	0.95	0.93	0.94	0.92
45/00/45 RMSE	136	125	109	2.14	1.96	0.2

non-symmetric cases in the equal-sense fold and two non-symmetric cases for the opposite-sense fold for two materials. These two materials are found to display similar behavior in both experimental and numerical data. A non-linear regression is applied to the full data set of each material assuming a simple second order polynomial, and the resulting fits are evaluated. Fits for the numerical data are not conclusively good, and therefore interpolation methods or a look-up table may be more appropriate for capturing these data trends, depending on needs. The regression is found to improve if smaller asymmetry ranges are used, or if the equal and opposite fold regimes are fit separately, so using a piecewise switching function is another possible solution. Experimental and numerical data predicting the hinge behavior in symmetric and non-symmetric folding are obtained. The results from these databases do not correlate and are not able to conclusively validate each other.

Recommendations for iterating on these results are to improve the testbed design to eliminate possible biases influencing the experimental data and to search for better candidate model functions for regression fits. A simpler test bed to investigate the symmetric data discrepancies only would be a good first step towards better understanding the results. Future work will focus on implementation of the hinge model into complex dynamics simulations and validation of the free deployment using the potential function.

VII Acknowledgments

This research was conducted under support from the NASA Space Technology Research Fellowship. The author would like to acknowledge support from the NASA Langley Research Center, from NASA collaborator Dr. Olive Stohlmann and from Dr. Juan Fernandez who provided the hinge materials and invaluable insight into the problem. Additionally, the author would like to thank Dr. Francisco Lopez-Jimenez for his support with ABAQUS.

References

- ¹Banik, J., *Frontiers of Engineering: Reports on Leading-Edge Engineering from the 2015 Symposium*, chap. Realizing Large Structures in Space, the National Academies Press, 2015.
- ²Jeon, S. K. and Footdale, J. N., "Scaling and Design of a Modular Origami Solar Array," *AIAA SciTech Spacecraft Structures Conference*, 2018.
- ³Pehrson, N. A., "Folding Approaches for Tensioned Precision Planar Shell Structures," *AIAA SciTech Spacecraft Structures Conference*, 2018.
- ⁴Thomson, M., Lisman, D., Helms, R., Walkemeyer, P., Kissil, A., Polanco, O., and Lee, S.-C., "Starshade Design for Occulter Based Exoplanet Missions," *Space Telescopes and Instrumentation 2010: Optical, Infrared, and Millimeter Wave*, 2010.
- ⁵Reynolds, W., Jeon, S., and Banik, J., "Advanced Folding Approaches for Deployable Spacecraft Payloads," *Proceedings fo the ASME 2013 International Design Engineering Technical Conference and Computers and Information in Engineering Conference*, Portland, OR, USA, August 4-7 2013.
- ⁶Kling, D., Jeon, S., and Banik, J., "Novel Folding Methods for Deterministic Deployment of Common Space Structures," *3rd AIAA Spacecraft Structures Conference*, 2016.
- ⁷Murphey, T. W. and Pellegrino, S., "A Novel Actuated Composite Tape-Spring for Deployable Structures," *45th AIAA/ASME/ASCE/AHS/ASC Structures, Structural Dynamics and Materials Conference*, 2004.
- ⁸Fulton, J. and Schaub, H., "Dynamic Modeling of Folded Deployable Space Structures With Flexible Hinges," *2017 AAS/AIAA Astrodynamics Specialist Conference*, Stevenson, WA, 2017.

⁹Blandino, J. R., Ross, B., Woo, N., Smith, Z., and McNaul, E., “Simulating CubeSat Structure Deployment Dynamics,” *AIAA SciTech Spacecraft Structures Conference*, 2018.

¹⁰Seffen, K. A. and Pellegrino, S., “Deployment dynamics of tape springs,” *Proceedings of The Royal Society of London*, 1998.

¹¹Soykasap, O., “Analysis of tape spring hinges,” *International Journal of Mechanical Sciences*, 2007.

¹²Walker, S. J. I. and Aglietti, G., “Study of the dynamics of three dimensional tape spring folds,” *AIAA Journal*, Vol. 42, No. 4, April 2004, pp. 850–856.

¹³Jain, A., *Robot and Multibody Dynamics*, Springer Science+Business Media, LLC, 2011.

VIII Appendix

Table 7: Reduced coefficients for the 45/0/45 FEA model

coefficient	M_{0_1}	M_{0_2}	M_{0_3}	N_{0_1}	N_{0_2}	N_{0_3}
a_1	-75.23	81.11	-10.95	0.5636	-	-0.1072
a_2	-	-15720	3964	-292.68	-44.10	-
a_3	-9706	14460	-10920	236.58	138.6	-2.215
a_4	453.3	-1122	565.5	-18.617	-7.337	-
a_5	-	803.8	-244.0	11.997	3.507	-
a_6	-	-	-	-	-	-0.01040
$b_{1,1}$	-	-	-	0.718	-	-
$b_{1,2}$	10850	10640	8842	175.3	-151.7	-
$b_{1,3}$	2192	-4310	5370	-71.58	-82.83	-
$b_{1,4}$	-131.9	-132	-	-2.224	-	0.0718
$b_{1,5}$	14.83	-	177.7	-	-2.988	0.1051
$b_{1,6}$	-0.7309	0.6111	-	-	-	-1.584E-3
$b_{2,2}$	-3590	19050	-	165.4	100.4	201.8
$b_{2,3}$	-	-	-10340	-	165.5	51.32
$b_{2,4}$	1004	-482.9	861.8	-8.875	-12.64	-2.091
$b_{2,5}$	-615.5	-	-467.3	-	8.655	3.075
$b_{2,6}$	178.1	141.25	173.5	2.845	-3.333	-0.08831
$b_{3,3}$	18140	-	-	-	-	-57.94
$b_{3,4}$	-	-	-	-	-	-1.499
$b_{3,5}$	396.7	-182.1	-	-	-1.551	-3.501
$b_{3,6}$	-101.7	157.3	110.0	2.843	1.312	-0.1451
$b_{4,4}$	11.47	3.916	-11.59	0.07821	0.1422	8.22E-3
$b_{4,5}$	10.42	-	5.962	-	-0.1010	-0.08333
$b_{4,6}$	1.777	-14.77	6.614	-0.2523	-0.08466	3.949E-3
$b_{5,5}$	-	-1.411	-	-	-	0.01146
$b_{5,6}$	-	9.077	1.981	0.1383	-0.04249	-
$b_{6,6}$	-	-0.008314	-	-6.74E-4	-	-1.087E-4

Table 8: Reduced coefficients for the 45/00/45 FEA model.

coefficient	M_{0_1}	M_{0_2}	M_{0_3}	N_{0_1}	N_{0_2}	N_{0_3}
a_1	-79	94.436	-8.423	0.5847	-	-0.05274
a_2	-	-10141	473.5	-198.3	4.435	-
a_3	-5319	7491.8	-7619	123.3	96.97	-2.749
a_4	314.3	-657.94	410.1	-11.42	-5.450	-
a_5	-	405.53	-213.8	6.627	3.428	-
a_6	-	-	-	-	-	-0.010411
$b_{1,1}$	-	-	-	0.9806	-	200.8
$b_{1,2}$	9392	7234.3	7088	135.9	-128.5	-
$b_{1,3}$	1669	-1949.5	1970	-29.98	-45.63	-
$b_{1,4}$	-124.6	-59.72	0	-1.383	-	0.1050
$b_{1,5}$	7.783	-	128.2	-	-2.482	0.07063
$b_{1,6}$	-0.834	0.9166	-	-	-	-7.06E-4
$b_{2,2}$	-3833	15600	-	106	152.3	16.60
$b_{2,3}$	-	-	-19880	-	217.5	65.83
$b_{2,4}$	602.6	-216.9	756.7	-4.278	-11.03	-2.537
$b_{2,5}$	-417.7	-	-493.4	-	9.328	4.643
$b_{2,6}$	197.7	205.8	101.9	3.926	-2.339	-0.0417
$b_{3,3}$	7078	-	-	-	-	0.003689
$b_{3,4}$	-	-	-	-	-	-3.581
$b_{3,5}$	263	-340.7	-	-	-1.971	1.006
$b_{3,6}$	-38.56	68.56	-115.8	1.493	1.158	-0.1696
$b_{4,4}$	-5.399	0.7478	-10.06	0.02931	0.1052	3.689E-3
$b_{4,5}$	6.6277	-	5.502	-	0.1007	-0.1366
$b_{4,6}$	0.2485	-10.12	5.318	-0.1835	-0.07294	2.662E-3
$b_{5,5}$	-	-3.420	-	-	-	0.07964
$b_{5,6}$	-	5.452	1.054	0.08784	-0.02882	-
$b_{6,6}$	-	-0.0158	-	-1.018E-3	-	-1.266E-4